Check for updates

Application of 3D printing for fabrication of superhydrophobic surfaces with reversible wettability†

Wenxuan Zhao,[a] Yanlong Zhan,*[b] Wen Li, [ID] *[a] Saisai Hao[a] and Alidad Amirfazli [ID] [ac]

Control of surface wettability is needed in many applications. The potential use of 3D printing technology to gain control over wettability remains largely unexplored. In this paper, Fused Deposition Molding (FDM) 3D printing technology was utilized to print polylactic acid (PLA) microplate array structures to generate superhydrophobic surfaces with reversable wetting properties. This was achieved by spraying polydimethylsiloxane (PDMS) and silica (SiO_2) solutions, over microplate surfaces. Anisotropic wetting properties were also achieved based on the surface structure design. Due to the shape memory properties of PLA, the morphology of the microplate arrays could be switched between the original upright shape and deformed shape. Through alternating pressing and heating treatments, the microplate arrays showed anisotropic wettability switching. The difference between the contact angle (CA) and sliding angle (SA) of water droplets on the original surface parallel to and perpendicular to the microplate array direction were $\Delta CA = 7°$ and $\Delta SA = 3°$ respectively, and those on the surface of the deformed microplate array were $\Delta CA = 7°$ and $\Delta SA = 21°$, respectively. This process enabled reversible alteration in the wetting behavior of water droplets on the original and deformed surfaces between sliding and sticking states. PLA-based shape memory anisotropic superhydrophobic surfaces with tunable adhesion were successfully applied to rewritable platforms, micro droplet reaction platforms, and gas sensing.

1. Introduction

Polymer 3D printing is an additive manufacturing technology that is best suited for manufacturing of complex geometric shapes; it has gained popularity in recent years due to its affordability, precision, and flexibility.[1–3] Fused deposition modeling (FDM) 3D printing technology builds parts layer by layer by extruding thermoplastic filaments.[4] Today, a wide range of polymer printing filaments are available to suit different product requirements, such as acrylonitrile butadiene styrene (ABS), PLA, high impact polystyrene (HIPS), thermoplastic polyurethane (TPU), and aliphatic polyamides (Nylon).[4–9] PLA stands out as the most commonly utilized material in 3D printing due to its favorable eco-friendliness, biodegradability, mechanical properties and shape memory properties.[10–12]

Superhydrophobic surfaces characterized by contact angle (CA) > 150° and sliding angle (SA) < 10° have a range of applications such as antimicrobial, droplet control, smart response,

and anti-icing.[13–17] Innovative approaches utilizing various 3D printing methods for fabricating such surfaces offer significant advantages over conventional techniques.[18] For example, Yang *et al.*[19] used 3D printing to prepare a bionic rose petal superhydrophobic surface with a micro-nano eggbeater structure, which allowed for adjustable surface adhesion, and could be as microscopic "hand" for droplet manipulation. Lee *et al.*[20] prepared a nanostructured hydrophobic coating using hydrophobic silica nanoparticles and PLA fibers by dip-coating process and FDM 3D printing technology, this process can be used for many applications such as liquid position control and low water adhesion. Yin *et al.*[21] realized adjustable wettability for droplet manipulation by 3D printing mushroom-like surface texture yielding superhydrophobic surfaces. Liu *et al.*[22] proposed 3D printing microscopic concave arrays for droplet adhesion, and tuning of macroscopic/microscopic droplet manipulation was shown by designing a variety of arrays.

Recently, related research on smart surfaces with dynamically switchable wettability in response to changes of an external stimuli have received extensive attention, especially for biomimetic structures. The transformation of surface chemical composition or geometrical structures determines the switchable characteristics of wettability. A large number of temperature-responsive surfaces with switchable wettability have been developed in recent years *via* grafting temperature-sensitive polymers. Poly(*N*-isopropylacrylamide) (PNIPAAm)

aSchool of Materials Engineering, Jiangsu University of Technology, Changzhou 213001, China. E-mail: lwjslg@126.com

bSmart Materials for Architecture Research Lab, Innovation Center of Yangtze River Delta, Zhejiang University, Jiaxing 314100, China. E-mail: l240086@zju.edu.cn

cDepartment of Mechanical Engineering, York University, Toronto, Canada

stands out as one of the most extensively studied and utilized for regulating surface wettability.[23,24] For example, Zhang et al.[25] fabricated a thermo-responsive PNIPAAm-modified nylon membrane via hydrothermal method. Furthermore, several researches on reversible superwetting transition were achieved by heat treatment and remodification, e.g., Zhang et al.[26] that designed a biomimetic switchable wetting surface on AZ91D Mg alloy.

The wettability of the surfaces fabricated by FDM 3D printing PLA can be finely tuned based on temperature-responsive shape memory mechanisms.[27–29] In this study, a thermal shape memory superhydrophobic surface with microplate structures was prepared. PLA served as the primary material to fabricate 3D printed microplate surface structures by FDM 3D printer, and a mixture of xylene, SiO_2, and PDMS was sprayed on the microplate structures to achieve a superhydrophobic layer. The anisotropic wettability of the superhydrophobic surfaces of the PLA microplate structure was investigated. The effect of ridge width and microplate spacing on the wettability was evaluated. The ability of controlling surface wettability through shape memory "switches" was also explored. The potential for the PLA shape memory superhydrophobic surfaces produced was shown for applications such as size-differentiated droplet grasping, droplet patterning, directional transport, and micro reaction platforms.

2. Experimental

2.1 Microplate array structure design by FDM 3D printing

The microplate array structures were made by FDM 3D printing (Utimer 3, Netherlands), using PLA filament (RAL 9010, 2.85 mm, Utimer, Holland). The process parameters were layer thickness of 0.25 mm, grid filling method, and print speed of 150 mm s^{-1}. The sample was prepared using computer-aided design (SolidWorks) to create the initial plate base (30 mm × 50 mm × 2 mm). The width, height, and spacing of the microplate array on the plate were 0.3 mm, 3 mm, and 0.78 mm, respectively, as shown in Fig. 1(a) and (b).

2.2 Preparation of superhydrophobic samples

PLA inherently possesses hydrophilic properties, as shown in Fig. 1(c) and (d). Consequently, the creation of superhydrophobic surfaces necessitates the application of additional hydrophobic layers along with micro and nanoscale structures.[30,31] After the microplate array samples were printed on top of the base plate, a spraying process was employed to modify both surface wettability and topography. Hydrophobic fumed silica nanoparticles (SiO_2, 12 nm, Evonik R974) and a mixture of PDMS (Sylgard184, Dow Corning Organic Silica Co., Ltd) and xylene (C8H10, Sinopharm Chemical Co., Ltd) were mixed to as pre-spray solution. By mixing SiO_2 : PDMS : xylene in a mass ratio of 0.5 : 1 : 20 and stirring for 3 h using a magnetic stirrer at 500 rpm, the mixture was ready for being sprayed on the microplate array surfaces. The spraying process was executed at a pressure of 0.6 MPa and a stand-off distance of approximately 30 cm. The spraying time lasted 5 s, and the sprayed samples

were dried at 22 °C room temperature for 1 h to obtain the PLA shape memory microplate array superhydrophobic surfaces. The sample preparation process was shown in Fig. 2.

2.3 Surface analysis

Scanning electron microscopy (FE-SEM, Novananosem, USA) and confocal microscopy (OLS4100, Olympus, Japan) were used to analyze the surface microscale and nanoscale morphologies of the samples. The coating is non-conductive and a metallic layer needs to be sprayed before testing, operating voltage 10 kV. The shape memory performance of the microplate array was analyzed using an intelligent thermostatic heating table (BY1010, BYA, China). The water droplet contact angle (CA) and the sliding angle (SA) were measured using a drop shape analysis (Krüss, DSA 30, Germany). A water droplet with a volume of 11 μL was used. The CA was measured by Young's fitting method. Measurements were performed in 5 different positions, and the average value was taken as the result of the CA and SA value.

3. Results and discussion

3.1 Surface anisotropic wettability of the microplate array

When the water droplets are placed on the superhydrophobic array surface, a continuous three-phase (solid–liquid–gas phase) contact line (TCL) is formed along the array direction. In contrast, the TCL is discontinuous in the direction perpendicular to the array due to the presence of microplate-induced energy barriers, and the length of the TCL is longer than that in the parallel direction.[32–34] Therefore, the water droplets are elongated in the parallel to the array direction and move more easily along such direction compared to the perpendicular direction. This results in a difference in CA and SA between the parallel and perpendicular to the array directions. For example, for water droplets on a microplate array with a space of 0.78 mm and a ridge width of 0.3 mm, the CA in the perpendicular direction ($CA_\perp$) was 160 ± 1.2°, while the CA in the parallel direction ($CA_\parallel$) was 153 ± 1.5° (Fig. 3(a)). SA in the perpendicular direction ($SA_\perp$) and SA in the parallel direction ($SA_\parallel$) were 7 ± 1° and 2.5 ± 1.5°, respectively (Fig. 3(b)). Both CA and SA measured perpendicular to the ridge were larger than those measured parallel to the ridge, showing anisotropic superhydrophobicity. The difference in wettability between parallel and perpendicular directions is mainly due to the oriented arrangement of anisotropic microplate structures on the surface.

The effects of 3D printed microplate array spacing (AS) and ridge width (RW) on surface wettability were investigated. The effect of array spacing on surface wettability was first measured at a ridge width of 0.39 mm. As seen in Fig. 3(a), the $CA_\perp$ and $CA_\parallel$ of water droplets with array spacing ranging from 0.38 mm to 1.58 mm showed a gradually decrease. Water droplets with array spacing ranging from 0.38 mm to 0.78 mm had a CA greater than 150° in the parallel direction, indicating superhydrophobicity. The $CA_\parallel$ with array spacing greater than 0.98 mm was 144°, so the superhydrophobicity was lost (as pre-
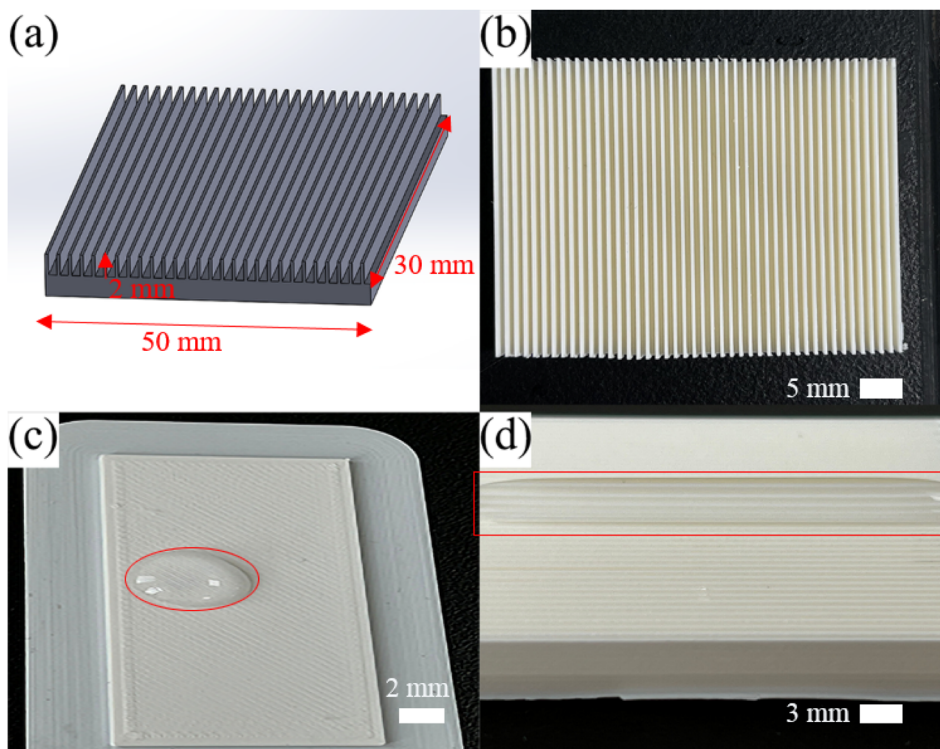
Fig. 1 (a) Solid works design model of the sample; (b) physical image of the sample; (c) optical images of a water droplet base plate with no microplates; and (d) with microplates are present on the surface. In (c) and (d) the red lines delimit the water drops.

conventional definition CA >150° and SA <10°). This was due to the fact that as the array spacing increased, the contact area between the droplet and the air also increased, and the droplet was seen to partially penetrated in the space between micro-plate array, resulting in a gradual decrease in CA. As seen in Fig. 3(b), the SA$_\parallel$ was always below 7° with array spacing ranging from 0.38 mm to 1.58 mm, which indicated that the droplet had excellent rolling performance along the array direction in parallel. The SA$_\perp$ showed a trend of first decreasing and then increasing around the array spacing of 0.78 mm. This was because as the array spacing increased, the contact area between the droplet and the surface also decreased. When the array spacing increased to a certain degree, the droplet was easily intruded in the microplate, which increased the rolling resistance of the droplet in the perpendicular direction and thus showed a higher SA. The CA of the array surface was the highest when the array spacing was 0.58 mm and it was most conducive to droplet sliding on the surface when the array spacing was 0.78 mm.

The effect of different ridge width arrays with array spacing of 0.58 mm and 0.78 mm on surface wettability was also investigated. As seen in Fig. 3(c), the CA$_\parallel$ of different ridge widths with array spacing of 0.58 mm and 0.78 mm exceeded 150°. Meanwhile, as seen in Fig. 3(d), the SA with array spacing of 0.58 mm and 0.78 mm increased with the increase of ridge width, which was attributed to the increase of ridge width can effectively increase the contact area between the surface and the droplet. When RW was 0.39 mm with array spacing of 0.78 mm, the SA in both perpendicular and parallel directions of array was smaller than that of array spacing 0.58 mm. The droplet had the best rolling performance on the array surface when RW was 0.3 mm. Therefore, the most favorable combination of array spacing and ridge width was determined to be 0.78 mm and 0.3 mm, respectively.
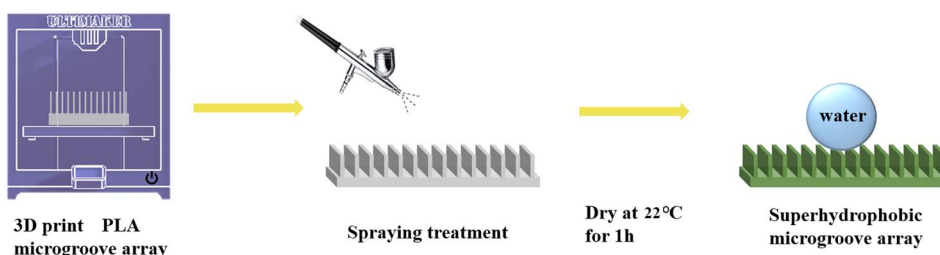

Fig. 2 Schematic diagram of superhydrophobic sample preparation.
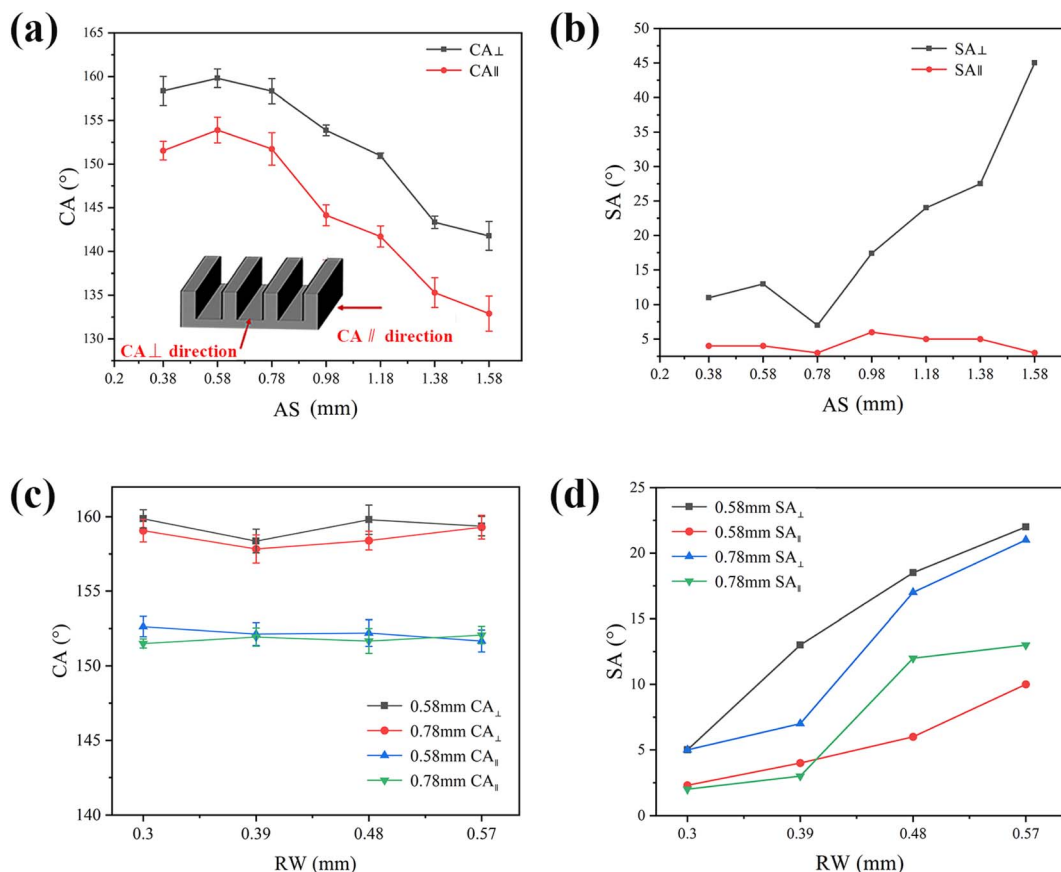
Fig. 3 Effect of different AS and RW on the surface wettability of the microplate array structure: (a) effect of different AS on the $CA_\perp$ and $CA_\parallel$ (the RW is 0.39 mm); (b) effect of different AS on the $SA_\perp$ and $SA_\parallel$ (the RW is 0.39 mm); (c) effect of different RW on the $CA_\perp$ and $CA_\parallel$ (the AS is 0.58 mm, 0.78 mm, respectively); (d) effect of different RW on the $SA_\perp$ and $SA_\parallel$ (the AS is 0.58 mm, 0.78 mm, respectively); lines are to guide the eye.

Fig. 4(a) showed the effect of bending angle (BA) on the wettability of microplate arrays. As bending angle α increases, $CA_\perp$ and $CA_\parallel$ gradually decrease, and the difference between $CA_\perp$ and $CA_\parallel$ always remains around 8°. In terms of sliding performance (a water droplet with a volume of 5 μL was used), when $\alpha < 15°$, water droplets easily slide on the sample surface. When α increases to 40° or above ($\alpha \leq 50°$), the SA in the direction of reverse deformation and SA in the direction of forward deformation dramatically increase to 90° and 80° with the water droplets pinning on the sample (Fig. 4(b)). The results show underscore the impact of α on water adhesion to the microplate structure's surface, that is, increasing the BA causes the surface to change from sliding state to sticky state. The optical image of the droplet depicted in Fig. 4(c1) illustrated the high adhesion of the droplet in both the reverse and forward deformation directions of the tilted microplate array. The sliding angle of the droplet, when measured in the reverse deformation direction of the microplate array, is greater than that measured in the forward deformation direction. Additionally, the droplet's resistance is directly proportional to the TCL when it slides on the solid surface, as depicted in Fig. 4(c2). The contact state of the droplet differs depending on whether it is moving along or against the tilted direction of the microplate array. When the droplet moves along the tilt direction, its tail contacts the top of the array, resulting in a shorter TCL length.

Conversely, when the droplet slides against the tilt direction, its tail contacts the side of the microplate array, leading to a longer TCL length. Consequently, the resistance of the droplet to rolling against the tilt direction of the microplate array is higher than when sliding along the tilt direction, resulting in different sliding angles.

Fig. 4(d) displayed the influence of the ridge height (RH) on the wettability of the microplate array. The sliding angle of the droplets for RH between 0.1 mm and 3 mm remains nearly unaffected by change in RH and less than 10°. The contact angle of the droplets on the other hand will increase by an increase in RH; at 0.1 mm of the RH the contact angle is 143°, whereas the contact angle of is greater than 155° when the RH is increased to more than 0.3 mm. The optical image of the droplet in Fig. 4(d) shows that when the RH is 0.1 mm, the droplet exhibited minimal contact with the inner wall of the ridge and the bottom of the microplate, existing in a coexistence state of Wenzel and Cassie. However, this configuration had relatively minimal influence on the droplet's sliding performance. With the increase of the RH the droplet is mainly in contact with the top of the ridge, and the air-filled grooves between the droplet and the microplate are seen. Eventually, the droplet transitions into a Cassie state, facilitating easy sliding on the microplate surface, and the contact angle exceeded 151°. The droplet exhibited enhanced sliding capability on the surface of the
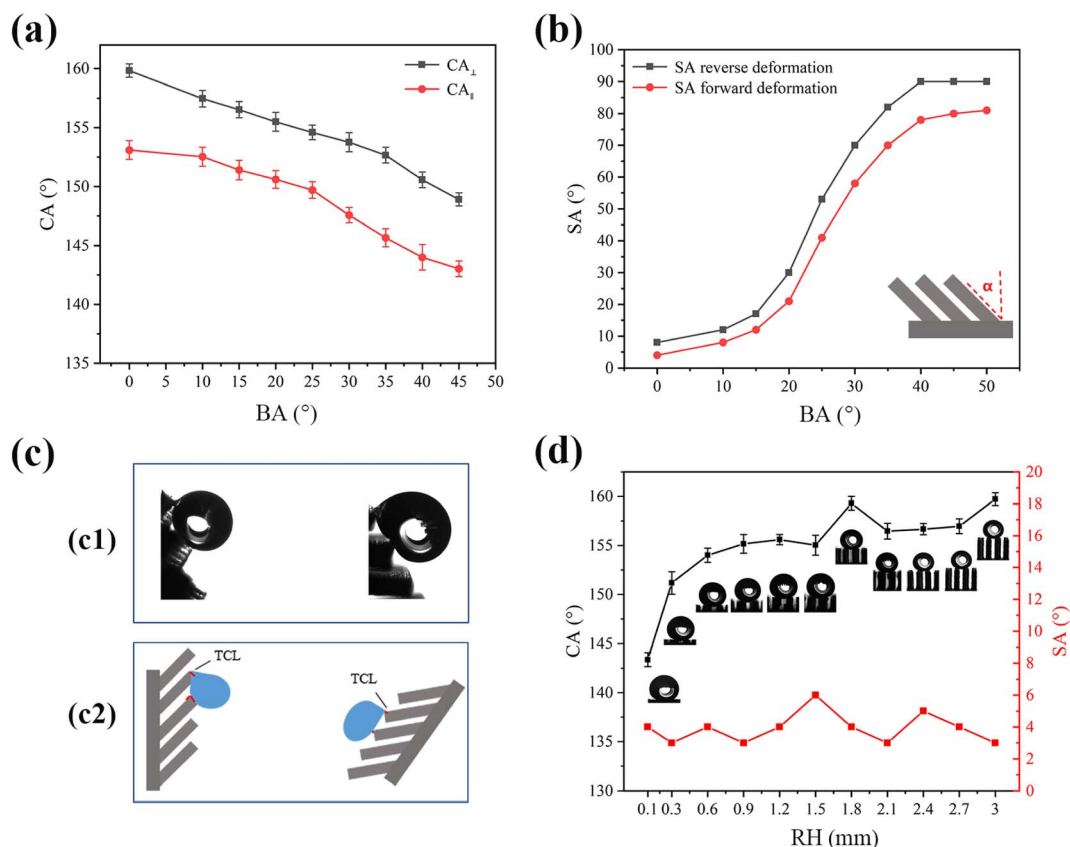
Fig. 4 Effect of different BA and RH on the surface wettability of the microplate array structure: (a) effect of different BA on the $CA_\perp$ and $CA_\parallel$; (b) effect of different BA on the SA in the direction of reverse deformation and SA in the direction of forward deformation; (c) schematic diagram of droplets sliding in different directions of the inclined array. (c1) Optical image, (c2) mechanism of movement; (d) effect of different RH on the CA and SA and optical images of droplets at different RH; lines are to guide the eye.

microplate. This behavior for an increasing contact angle is consistent with thermodynamics analysis of similarly structured surfaces for Cassie wetting state.[35]

3.2 Shape memory properties of PLA microplate

PLA is a semi-crystalline polymer, and the differential scanning calorimetry (DSC) analysis of PLA, see Fig. 5, PLA first underwent glass transition at 40–80 °C, and then crystallized and
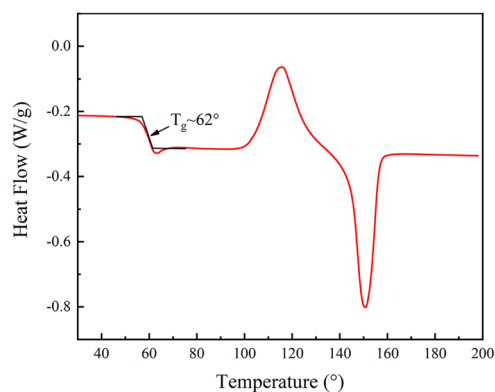

Fig. 5 Differential scanning calorimetry (DSC) analysis curve for SM-PLA.

melted at 90–180 °C. The glass transition temperature of the specimen was determined to be approximately 62 °C using the equidistant method, which implies that the phase state of the polymer can be changed from glassy state to rubbery state when the temperature is above 62 °C. As such, in our experiments, 80 °C was selected to soften the sample. So, to investigate the shape memory (SM) properties, we first heat the table to 80°, then put the SM microplate sample on the heating platform for three minutes, and remove the microplate after it becomes soft. A 2 kg weight was placed on the softened microplate array to bend the SM microplate array. An alternate method of using a glass rod to push the microplate could also be used to bend and deform the microplate (the glass rod should remain in contact during cooling process to ensure deformation) a schematic diagram of the reversible morphological transformation of the microplate array is shown in Fig. 6(a).

The SM microplate exhibited noticeable macroscopic shape memory effects, see Fig. 6(b) and (c). Laser confocal microscopy was employed to study the changes of the microplate array during deformation and recovery, see Fig. 6(e–g). The morphology and dimensions of the arrays observed in the confocal microscopy images were in good agreement with the physical images. The height of the original ridge was 3 mm. External pressure caused the ridge to tilt to one side in an
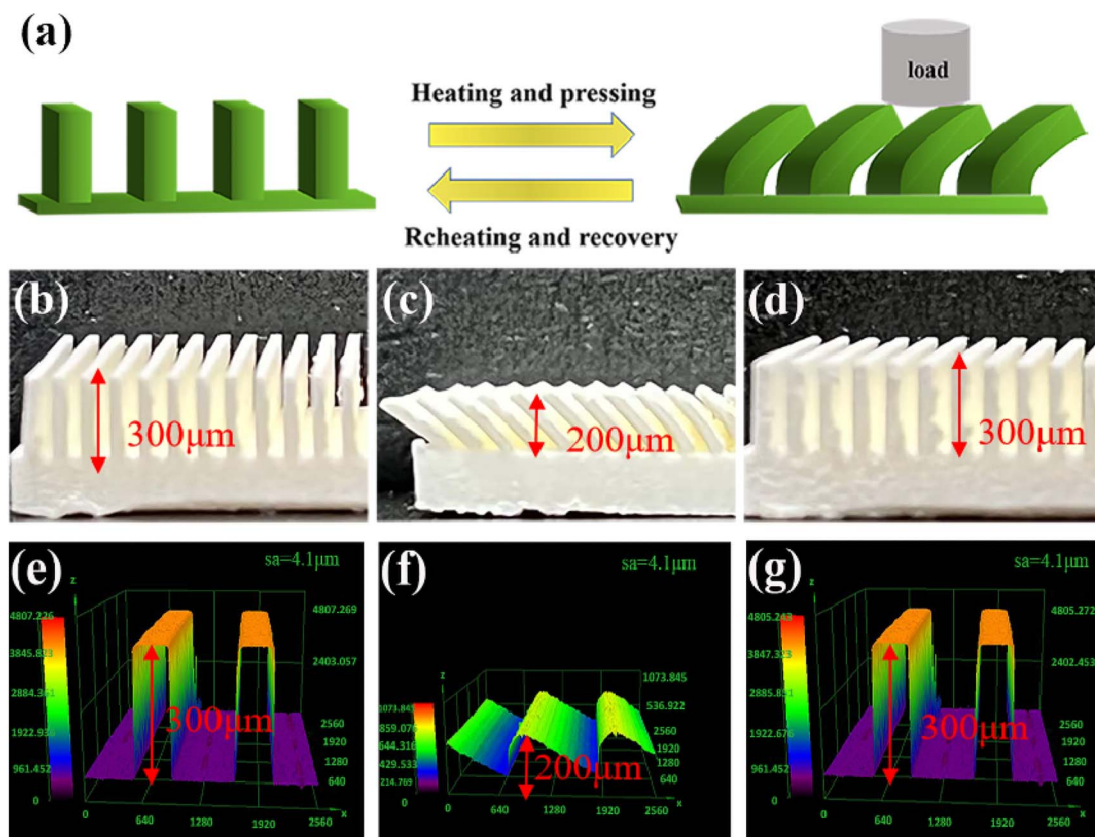
Fig. 6 (a) Schematic diagram of the reversible morphological transition between the original state and the deformed state; (b–d) are the physical images of the original, deformed, and restored microplate arrays, respectively; (e–g) are the 3D confocal microscopy images of (b–d), respectively, and the array heights are consistent with the physical images.

orderly manner, thus reducing the height of the ridge by 1 mm shown in Fig. 6(c) and (f). However, following the reheating process, the tilted ridge morphology and dimensions were restored to their original state, as shown in Fig. 6(d) and (g). The roughness of the coating surface was analyzed with confocal microscopy and the average surface roughness of the coating was 4.1 μm, as shown in Fig. 6(e)–(g).

Fig. 7(a) showed the SEM images of the surface of the prepared SM microplate original array. A regular microplate array with a ridge width of 0.3 mm can be seen. After heating at 80 °C for 2 min on shear deformation of the microplate array, it can be seen that the SM microplate array show uniform deformation (Fig. 7(b)). In addition, the micron-level structure of the top and side walls of the microplate surface ridge was not significantly altered to affect the wettability of the SM microplate surface. When the deformed SM microplate arrays were reheated at 80 °C for about 3 min, the shape and orientation of the microplate arrays were almost completely restored to original state (Fig. 7(c)). Fig. 7(d) shows that the top surface of the ridge of the blank microplate array is smooth and flat, Fig. 7(e) shows that the superhydrophobic coating is uniformly and densely distributed on the top and side wall surfaces of the microplate array, and Fig. 7(f) shows the spherical particle topography of the array surface formed by SiO_2 particles, and the PDMS-coated hydrophobic SiO_2 forms a micron-scale circular protrusion structure with a diameter of about 1–10 μm at the top of the ridge. As seen in Fig. 7(g), the ridge side walls had a clear layered structure due to the FDM 3D printer XZ direction, which was a laminar structure generated by layers of stacked fused print filaments, also containing micron-sized protruding structures formed by PDMS-coated hydrophobic SiO_2. Fig. 7(h) and (i) shows that the micron-scale structure of the surface of the array after deformation and recovery is not affected, and the coating surface is uniform and does not fall off significantly. Fig. 7(j) of the microplate array shows that the average thickness of the coating is 42 μm. Fig. 7(k) and (l) is the EDS analysis of SM superhydrophobic microplate surface, Fig. 7(k) is the surface composition of the blank array, the surface composition of the original array is the main component of PLA, mainly composed of C, O and H elements, compared with the blank array, the content of O and Si elements increases significantly, and the content of C elements decreases, which proves the successful introduction of SiO_2/PDMS coating on the surface.

3.3 Reversible wettability and mechanism of SM microplate surfaces

The wettability of the SM microplate surfaces can be switched by the heating process, see Fig. 8(a) and (b). When water droplets are placed on the surface of the original prepared
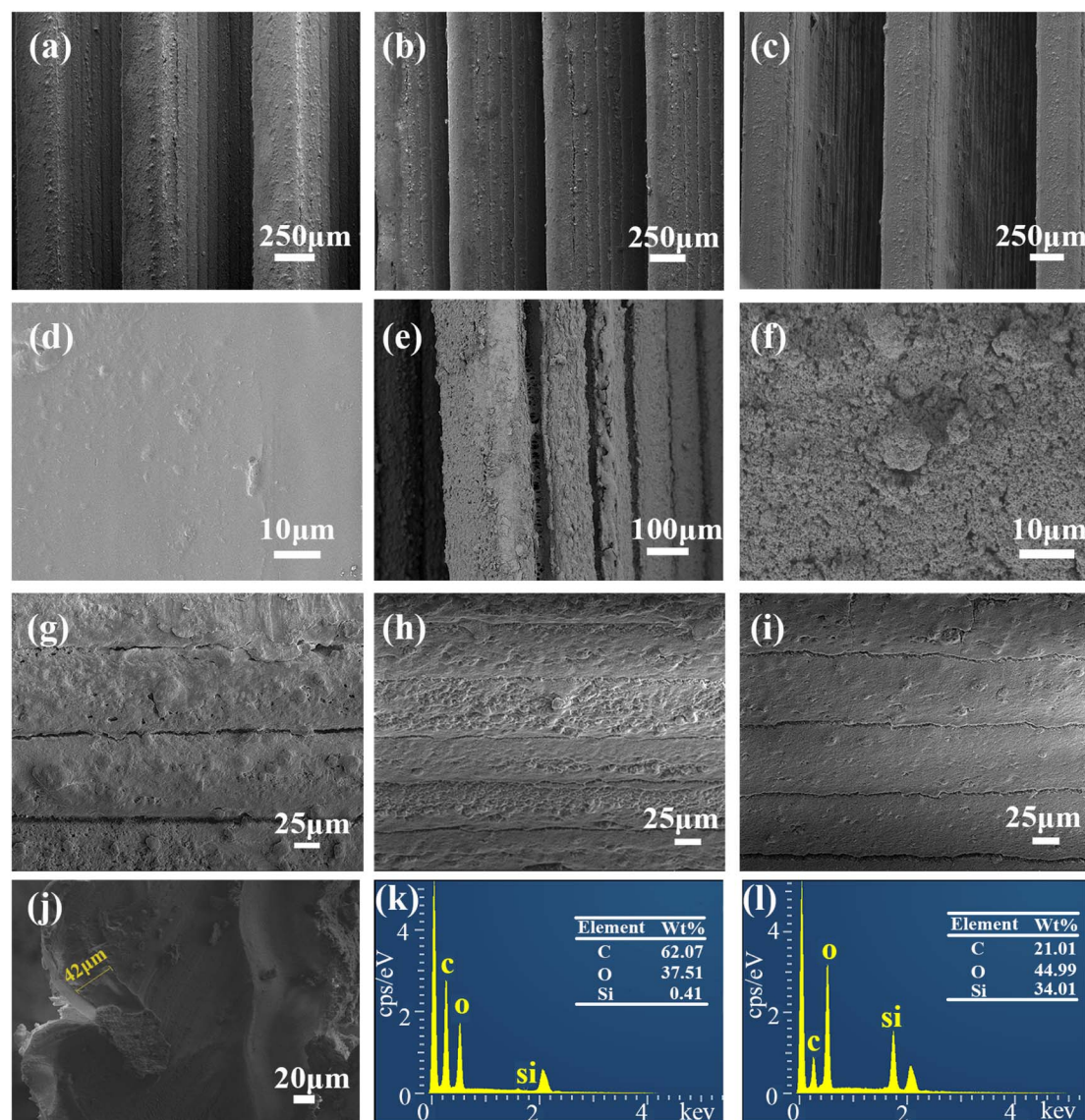
Fig. 7 (a–c) SEM images of the (a) original SM microplate arrays, (b) microplate arrays after deformation, (c) microplate arrays after recovery. (d–f) SEM images of the (d) Blank SM microplate ridge, (e and f) SM superhydrophobic microplate ridge. (g–i) Magnified SEM images of the side walls of the microplate array ridge for (a)–(c), respectively. (j) Cross-sectional image of the SM superhydrophobic microplate ridge. (k and l) EDS image of the (k) blank SM microplate ridge, (l) SM superhydrophobic microplate ridge.

shape memory microplate, "air cushion" between the water droplets and the microplate array can be clearly observed along the microplate direction (Fig. 8(c)). At this point, the original array surface exhibited low adhesion, superhydrophobicity and anisotropic wettability ($CA_{\parallel} = 153 \pm 1.5°$, $CA_{\perp} = 160 \pm 1.2°$, $SA_{\parallel} = 2.5 \pm 1°$, $SA_{\perp} = 5 \pm 1.5°$), see Fig. 8(c). After deformed, all microplates were tilted to one side with a bending angle of about 48° and $CA_{\parallel}$ decreased to $143 \pm 1.3°$, $CA_{\perp}$ decreased to $150 \pm 1.5°$ on the tilted microplate (Fig. 8(c)). The difference between $CA_{\perp}$ and $CA_{\parallel}$ was about 7° and the deformation surface can still maintain anisotropic wettability. The $SA_{\parallel}$ increased to $8 \pm 1.3°$, and $SA_{\perp}$ increased to $26 \pm 1.5°$ (Fig. 8(c)), indicating that the droplet rolled differently in the two directions. By alternately pressing and heating the treatment reversibly for 10 cycles, the CA and SA showed similar values for each cycle, see Fig. 8(a) and (b). This demonstrated high controllability and reproducibility of anisotropic, switchable adhesion of thermally prepared responsive superhydrophobic surfaces.

To further understand the relationship between the structure of SM surface and its corresponding wettability, a possible mechanism was elucidated in Fig. 9. In general, SM have two components: shape fixation and shape transformation components. The shape fixation component or dot is responsible for maintaining dimensional stability during deformation and recovery, and the shape transformation component consists of long polymer chains that store elastic energy.[36–38]

For the thermo-responsive PLA SM in our experiments, the long PLA chains acted as shape transformation component and their physical entanglements acted as permanent networks.[39]
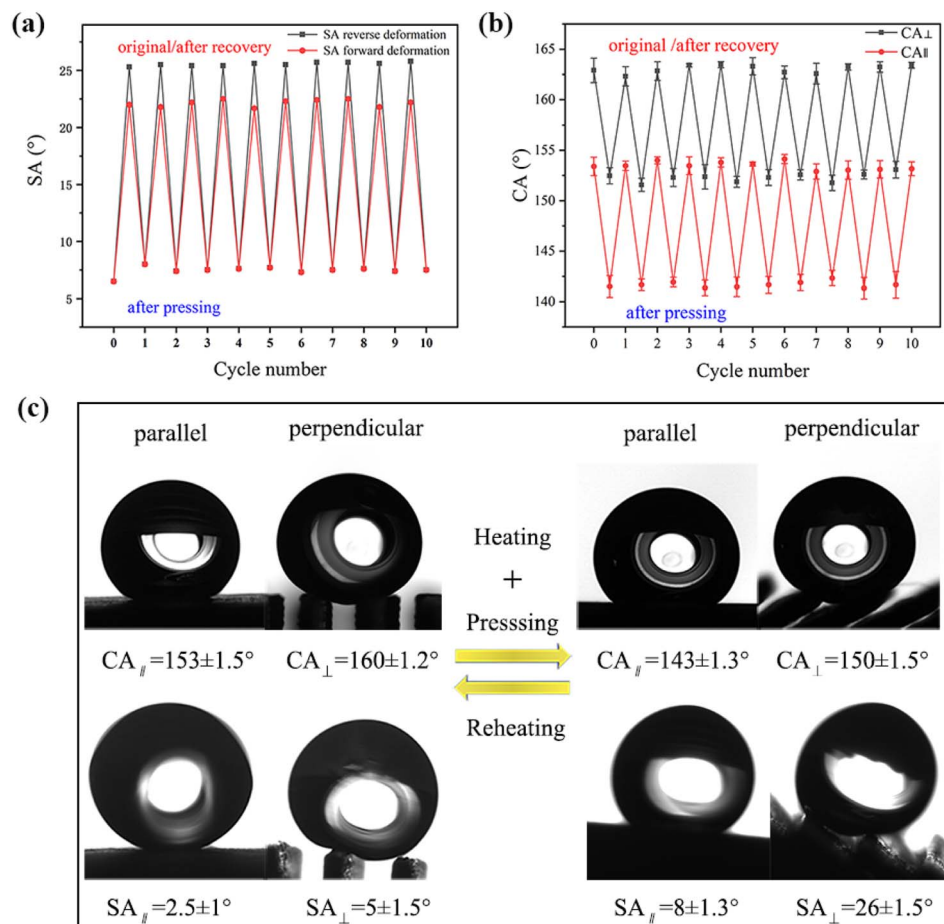
Fig. 8 Reversible changes of (a) SA along the deformation direction and opposite direction, (b) CA $_\perp$ and CA $_\parallel$, and (c) perpendicular and parallel array direction CA, SA (SA $_\perp$ is against the tilt direction) images on the SM microplate array by repeating the pressing and recovery process; in (a) and (b) lines are to guide the eye.

Initially, the microplate arrays of the SM were in their original shape (Fig. 9(c)), where the molecular chain conformation had the highest entropy and is in a thermodynamically stable state (Fig. 9(a)). The water droplets were in contact only with the top of the ridge which had a micro-nano structure, forming a discontinuous and short TCL. The strong repulsive forces existed at the gas–liquid contact surface, causing the water droplets to adopt a Cassie state.[40] Therefore, the surface showed low adhesion. However, when the SM microplate array was heated at temperatures higher than T_g (~62 °C), the polymer chains between the physical entanglements of the long PLA chains were activated, at this time, the molecular conformation shifted to a non-equilibrium state, and the microplate arrays can be easily deformed under the action of the external forces (Fig. 9(d)). Upon cooling, the motion of the molecular chains was frozen, and the deformed shape was fixed in a low-entropy non-equilibrium state (Fig. 9(b)). At this time, the microplate array was tilted and fixed to a temporary shape (Fig. 9(e)), and the contact area between the droplets and the sidewalls of the microplates increased compared with that of the upright microplates, forming a continuous and elongated TCL. The wetting state was consistent with the transition state between the Wenzel state and the Cassie state.[41] The increase in contact

area and TCL length lead to an increase in adhesion on the deformed array surface. When reheating the deformed SM at temperatures higher than T_g, the fixed molecular chain movements were reactivated. The entropic energy stored in the deformed polymer chains was released, and therefore the deformed shape returned to its original state (Fig. 9(f)). Correspondingly, the surface wettability of the microplate-structured SM was also restored to its original state.

3.4 Application of shape memory superhydrophobic surfaces

By exploiting the switchable adhesion and anisotropic wettability of SM surfaces, multiple droplet manipulation-related applications can be reproducibly and selectively realized on the superhydrophobic surfaces. When a 15 μL droplet was placed on the pristine superhydrophobic surface (stained by methyl blue for observation), the droplet slid easily (Fig. 10(a1–a3)), movie s1 in ESI†). When the microplate surface was pressed so that the array was tilted, large droplets with droplet volumes greater than 12 μL slid easily along the parallel array direction (Fig. 10(b1–b3)), movie s2 in ESI†), and in the perpendicular array direction large droplets slid with difficulty.
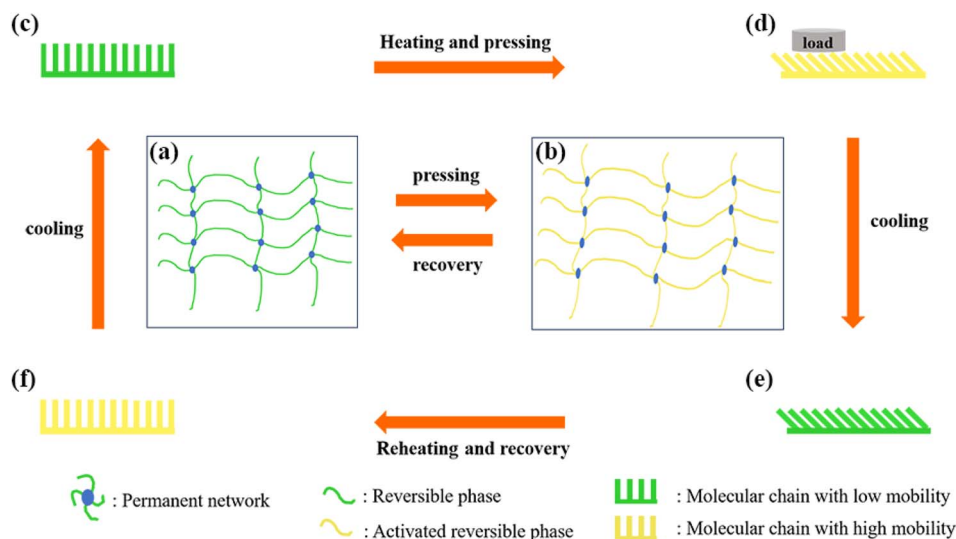
Fig. 9 (a and b) Schematic diagrams of the reversible transformation process of the molecular chain configuration of SM polymers in the pristine and deformed states: (a) the pristine SM polymers structure contains a large number of dots and the molecular chain configuration with the highest entropy, and (b) the deformed SM polymers structure consists of a large number of dots and the molecular chain with a lower entropy. (c–f) Schematic diagrams of the shape memory process of SM polymers microplate arrays: (c) pristine upright microplate arrays, (d) microplate arrays that can be deformed when the temperature is heated above the T_g temperature and squeezed by an external force, (e) tilted microplate arrays after cooling, and (f) deformed microplate arrays that recover when the temperature is heated up to the T_g again and revert to the pristine upright microplate arrays after cooling.
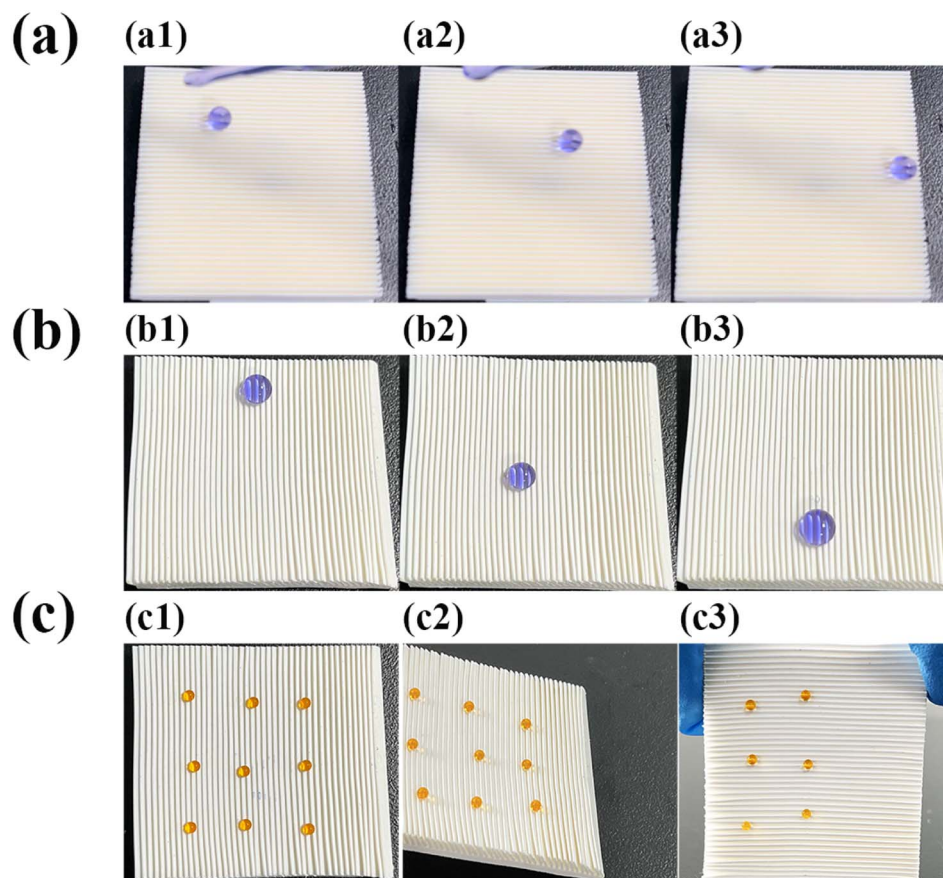

Fig. 10 Rolling state of water droplets on shape memory microplate array superhydrophobic surfaces. (a1–a3) The process of droplets sliding in a disordered manner on the pristine microplate array superhydrophobic surfaces. (b1–b3) Droplets with a droplet volume greater than 12 μL on tilted microplate array tend to slide along the microplates. (c1–c3) Droplets with a droplet volume less than 7 μL were pinned on the tilted microplate array surface with a tilted angle of 0°, 30° and 90°, respectively.

While small droplets with droplet volumes less than 7 μL (stained by methyl orange to distinguish form large droplets) exhibited a tendency to pin along the opposite array tilting direction. This pinning phenomenon of small droplets to the tilted microplate arrays superhydrophobic surface were shown in Fig. 10(c) (Fig. 10(c1–c3)) for 6 μL droplets pinned to flat, tilted at 30°, and tilted at 90° on SM microplate array panels, respectively). This phenomenon was attributed to the fact that the driving force generated by gravity of smaller droplets was smaller than the resistance generated by the microplate array, which resulted in the droplets pinning on the array surfaces.[42]

When a portion of the microplate arrays was deformed, the SM microplate array acted as a "switch" and the deformed area turned into a high adhesion state. For example, the SM arrays were first heated at 80 °C for 3 min, and then a "*T*" pattern was pressed using a glass rod, and after cooling to room temperature, a 10 μL droplet could only stay on the "*T*" pattern where microplates were deformed (Fig. 11a1). Upon reheating the patterned deformed SM at 80 °C, the deformed arrays were restored to the original state. It was possible to rewrite other patterns, such as "<" (Fig. 11a2), and "\" (Fig. 11a3) on the SM surface. When a droplet dropped at the top of the inclined 3° "\" track, it rolled rapidly down the track (Fig. 11b1–b3, movie s3 in ESI†).

The results demonstrated that the rewritable tracks on the SM superhydrophobic surface can be strategically oriented to guide the droplet transport. More interesting was to utilize the
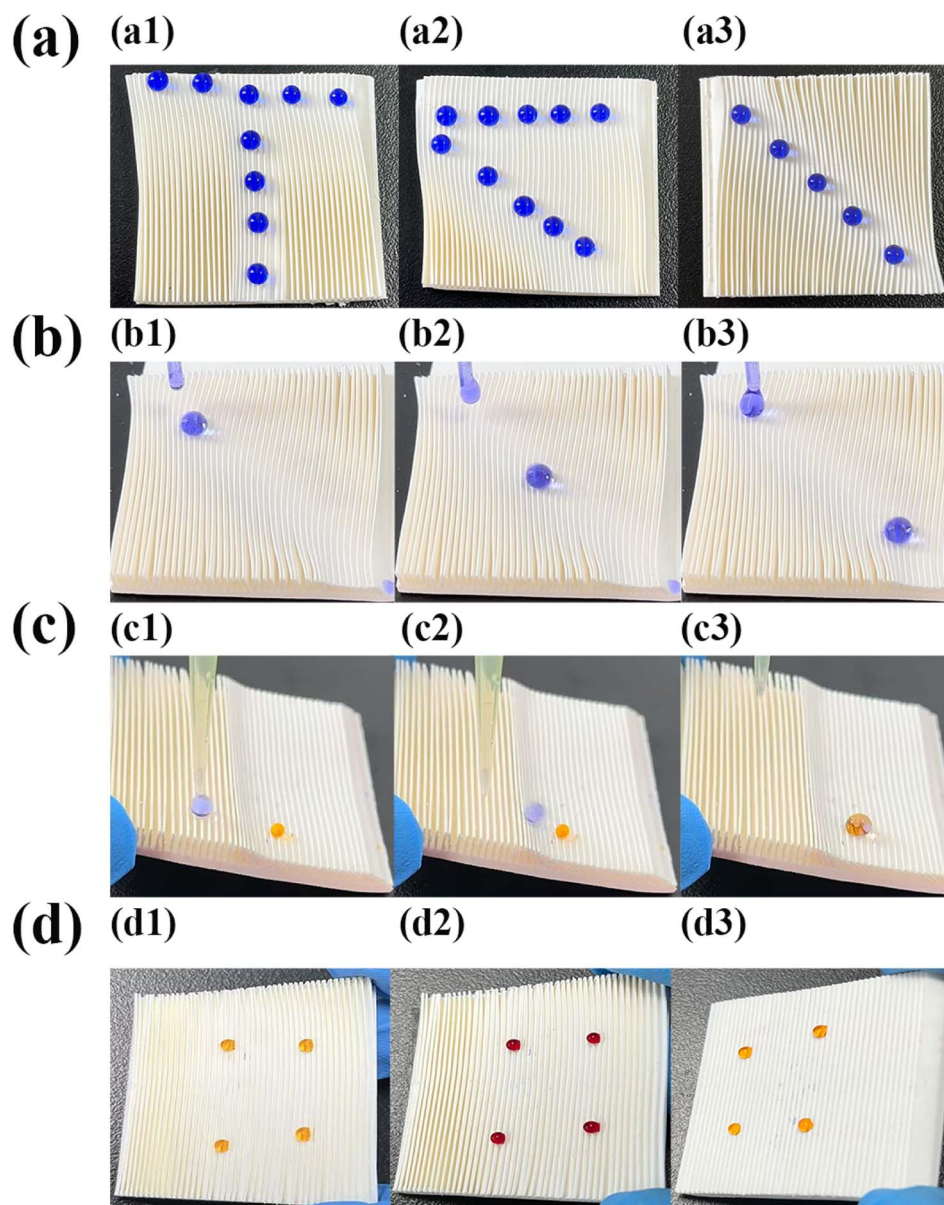

Fig. 11 (a1–a3) Droplets can only be placed on the deformed SM microplate array, (a1) "*T*" (a2) "<" (a3) "\". (b1–b3) The process of directional transportation of droplets on the surface of SM microplate arrays. (c1–c3) Mixing process of methyl blue solution and methyl orange solution. (d1–d3) (d1) Pristine phenol red solution droplets arranged on the deformed region of the micromicroplate array, (d2) treated with NH₃ gas, and (d3) further treated with HCl gas.

"switching property" of the microplate superhydrophobic surface as a micro-reaction platform. As shown in Fig. 11c1, a drop of 5 μL methyl orange droplet was placed on one side of the deformed microplate arrays, and then a drop of 10 μL methyl blue droplet was placed on one side of the pristine microplate arrays (Fig. 11c2), and it can be seen that the methyl blue solution rolled towards the methyl orange solution and the two solutions coalesced and adhered to the side of the deformed areas (Fig. 11c3, movie s4 in the ESI†). In addition, liquid–gas microchemical reactions can be carried out on the patterned surface.[43]

The tilted SM microplate arrays were highly adherent to small droplets. Dynamically stable droplet arrays with multi-sensing indication are well suited for gas sensing by colorimetric reactions on the surface of high-adhesion SM microplate arrays. For example, qualitative NH_3 and HCl gas sensing experiments. Four drops of 7 μL phenol red solution was placed on a tilted SM arrays at 30° to form a stable gas-sensitive microarray (Fig. 11d1), when the platform is exposed to NH_3 gas, it can be seen that the phenol droplets turn red (Fig. 11d2), after a simple on-chip qualitative test, the droplets still adhere to the surface of the microplate without changing color. The droplets did not penetrate into the microplates or rolling off, therefore, the droplets can still be sensed and analyzed. Next, the microplate platform was exposed to HCl gas, due to the high sensitivity of the phenol red solution to pH changes, the phenol red droplets changed color from red to yellow (Fig. 11d3). This phenomenon was due to the high sensitivity of the phenol red solution to pH changes. Compared to other highly adhesive platforms, the SM array platform can recovered and be reused. These results suggest that droplet arrays on the surface of highly adhesive inclined SM microplates can be used as an analytical device for convenient and rapid colorimetric analysis over a wide range of concentrations for a low cost due to a fewer reagent volume requirements.

3.5 Prospects for FDM 3D printing superhydrophobic surfaces

Many superhydrophobic material preparation use fluorine-containing materials or organic solvents; such techniques are increasingly raising concerns regarding health (fluorine). The traditional preparation methods are also sometimes complex and multistep processes, especially, if specific patterns are need to be generated. FDM 3D printing technology can address the issues stated above. The use of PLA, which is a degradable and renewable green material, makes FDM printing for making superhydrophobic with specific surface texture, *e.g.*, see Fig. 12, especially appealing. This work demonstrates such idea that is largely unexplored to date. We also show how FDM 3D printing technique can be a flexible multi-material method to generate superhydrophobic surfaces. This is shown as we prepared the microplate structure, first in PLA for large surface features, and the continued the printing using ABS for finer features to achieve desired wettability outcome. ABS has high strength and good toughness, that can support longevity of surface due to contact, as shown in Fig. 12(a and b). Fig. 12 (c–f) shows several examples of 3D-patterned superhydrophobic surfaces designed
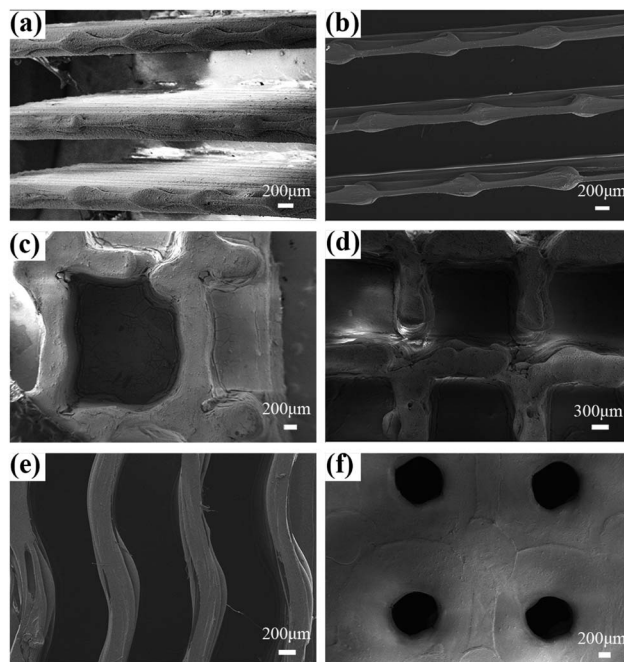

Fig. 12 Various 3D printed superhydrophobic microstructure surfaces.

for 3D printing, allowing one to explore the influence of surface structure on the wettability. Taken all together, the idea of using FDM, in a multi-material format and with SM properties is a unique aspect of this work that has also been highlighted through a demonstrative application.

4. Conclusions

In conclusion, this study showed the innovative fabrication of smart shape-memory superhydrophobic surfaces through 3D printing, demonstrating capabilities for anisotropic wettability and adhesion modulation. The wettability can be regulated by varying the microplate AS, RW and BA. Specifically, the microplate structure surface with AS of 0.78 mm and RW of 0.3 mm showed anisotropic wettability and low adhesion superhydrophobicity against water droplets with $CA_\parallel$ of $153 \pm 1.5°$, $CA_\perp$ of $160 \pm 1.2°$, $SA_\parallel$ of $2.5 \pm 1°$, and $SA_\perp$ of $5 \pm 1.5°$. Remarkably, both the surface morphology and wettability can be fully recovered by a simple reheating process. This deformation/recovery process can be repeated for at least 10 cycles without any decreasing of the superhydrophobicity due to shape memory effect of PLA. Based on switchable adhesion, the microplate-structured super-hydrophobic surfaces serve as versatile platforms for droplet manipulation. Such as size-discriminative gripping droplets, droplet patterning, directional transport, and micro-reaction platforms for droplets. We believe that PLA-based SM super-hydrophobic surfaces will have a wide range of applications in droplet control, microfluidic field, and switchable wettability.

Conflicts of interest

There are no conflicts to declare.

Acknowledgements

References

1 Z. X. Khoo, J. E. M. Teoh, Y. Liu, C. K. Chua, S. Yang, J. An, K. F. Leong and W. Y. Yeong, *Virtual Phys. Prototyping*, 2015, **10**, 103–122.

2 A. Savini and G. Savini, *2015 ICOHTEC/IEEE International History of High-Technologies and their Socio-Cultural Contexts Conference (HISTELCON)*, **2015**, pp. 1–8.

3 Y. Ding, J. Sun, H. W. Ro, Z. Wang, J. Zhou, N. J. Lin, M. T. Cicerone, C. L. Soles and S. Lin-Gibson, *Adv. Mater.*, 2011, **23**, 421–425.

4 P. Dudek, *Arch. Metall. Mater.*, 2013, **58**, 1415–1418.

5 C. S. Lee, S. G. Kim, H. J. Kim and S. H. Ahn, *J. Mater. Process. Technol.*, 2007, **187–188**, 627–630.

6 Y. He, G. H. Xue and J. Z. Fu, *Sci. Rep.*, 2014, **4**, 6973.

7 S. Yuan, F. Shen, J. Bai, C. K. Chua, J. Wei and K. Zhou, *Mater. Des.*, 2017, **120**, 317–327.

8 Y. Kim, C. Yoon, S. Ham, J. Park, S. Kim, O. Kwon and P. J. Tsai, *Environ. Sci. Technol.*, 2015, **49**, 12044–12053.

9 J. Madamesila, P. McGeachy, J. E. Villarreal Barajas and R. Khan, *Phys. Med.*, 2016, **32**, 242–247.

10 F. S. Senatov, M. Y. Zadorozhnyy, K. V. Niaza, V. V. Medvedev, S. D. Kaloshkin, N. Y. Anisimova, M. V. Kiselevskiy and K.-C. Yang, *Eur. Polym. J.*, 2017, **93**, 222–231.

11 F. S. Senatov, K. V. Niaza, M. Y. Zadorozhnyy, A. V. Maksimkin, S. D. Kaloshkin and Y. Z. Estrin, *J. Mech. Behav. Biomed. Mater.*, 2016, **57**, 139–148.

12 A. Lendlein and R. Langer, *Science*, 2002, **296**, 1673–1676.

13 Y. Zhan, W. Li, A. Amirfazli and S. Yu, *Polymer*, 2022, **256**, 125193.

14 Y. Zhan, S. Yu, A. Amirfazli, A. Rahim Siddiqui and W. Li, *Adv. Eng. Mater.*, 2022, **24**, 2101053.

15 Y. Zhan, S. Yu, A. Amirfazli, A. R. Siddiqui and W. Li, *Adv. Mater. Interfaces*, 2022, **9**, 2102010.

16 W. Li, Y. Zhan, A. Amirfazli, A. R. Siddiqui and S. Yu, *Prog. Org. Coat.*, 2022, **168**, 106877.

17 W. Li, Y. Zhan and S. Yu, *Prog. Org. Coat.*, 2021, **152**, 106117.

18 R. Jafari, C. Cloutier, A. Allahdini and G. Momen, *Int. J. Adv. Des. Manuf. Technol.*, 2019, **103**, 1225–1238.

19 Y. Yang, X. Li, X. Zheng, Z. Chen, Q. Zhou and Y. Chen, *Adv. Mater.*, 2017, **30**, 1521–4095.

20 K.-M. Lee, H. Park, J. Kim and D.-M. Chun, *Appl. Surf. Sci.*, 2019, **467–468**, 979–991.

21 Q. Yin, Q. Guo, Z. Wang, Y. Chen, H. Duan and P. Cheng, *ACS Appl. Mater. Interfaces*, 2021, **13**, 1979–1987.

22 X. Liu, H. Gu, M. Wang, X. Du, B. Gao, A. Elbaz, L. Sun, J. Liao, P. Xiao and Z. Gu, *Adv. Mater.*, 2018, **30**, e1800103.

23 Y. Liu, S. Tas, K. Zhang, W. M. de Vos, J. Ma and G. J. Vancso, *Macromolecules*, 2018, **51**, 8435–8442.

24 B. Su, W. Guo and L. Jiang, *Small*, 2015, **11**, 1072–1096.

25 W. Zhang, N. Liu, Q. Zhang, R. Qu, Y. Liu, X. Li, Y. Wei, L. Feng and L. Jiang, *Angew. Chem., Int. Ed.*, 2018, **57**, 5740–5745.

26 D. Zang, R. Zhu, W. Zhang, X. Yu, L. Lin, X. Guo, M. Liu and L. Jiang, *Adv. Funct. Mater.*, 2017, **27**, 1605446.

27 X. Bai, Q. Yang, Y. Fang, J. Zhang, J. Yong, X. Hou and F. Chen, *Chem. Eng. J.*, 2020, **383**, 123143.

28 G. Kaur, A. Marmur and S. Magdassi, *Addit. Manuf.*, 2020, **36**, 101669.

29 Y. Wang, H. Lai, Z. Cheng, H. Zhang, Y. Liu and L. Jiang, *ACS Appl. Mater. Interfaces*, 2019, **11**, 10988–10997.

30 P. Pi, W. Mu, G. Fei and Y. Deng, *Appl. Surf. Sci.*, 2013, **273**, 184–191.

31 G. Y. Bae, J. Jang, Y. G. Jeong, W. S. Lyoo and B. G. Min, *J. Colloid Interface Sci.*, 2010, **344**, 584–587.

32 D. Xia, L. M. Johnson and G. P. Lopez, *Adv. Mater.*, 2012, **24**, 1287–1302.

33 J. Yong, Q. Yang, F. Chen, D. Zhang, U. Farooq, G. Du and X. Hou, *J. Mater. Chem. A*, 2014, **2**, 5499–5507.

34 F. Gao, Y. Yao, W. Wang, X. Wang, L. Li, Q. Zhuang and S. Lin, *Macromolecules*, 2018, **51**, 2742–2749.

35 W. Li and A. J. A. i. c. Amirfazli, i, *science*, 2007, **132**, 51–68.

36 J. Xu and J. Song, in *Shape Memory Polymers for Biomedical Applications*, 2015, pp. 197–217, DOI: DOI: **10.1016/b978-0-85709-698-2.00010-6**.

37 W. M. Huang, H. B. Lu, Y. Zhao, Z. Ding, C. C. Wang, J. L. Zhang, L. Sun, J. Fu and X. Y. Gao, *Mater. Des.*, 2014, **59**, 176–192.

38 C. Renata, W. M. Huang, L. W. He and J. J. Yang, *Journal of Mechanical Science and Technology*, 2017, **31**, 4863–4873.

39 B. Tyler, D. Gullotti, A. Mangraviti, T. Utsuki and H. Brem, *Adv. Drug Delivery Rev.*, 2016, **107**, 163–175.

40 A. B. D. Cassie and S. Baxter, *Trans. Faraday Soc.*, 1944, **40**, 546–551.

41 T. Koishi, K. Yasuoka, S. Fujikawa, T. Ebisuzaki and X. C. Zeng, *Proc. Natl. Acad. Sci. U. S. A.*, 2009, **106**, 8435–8440.

42 E. Pierce, F. J. Carmona and A. Amirfazli, *Colloids Surf., A*, 2008, **323**, 73–82.

43 J. Y. Huang, Y. K. Lai, F. Pan, L. Yang, H. Wang, K. Q. Zhang, H. Fuchs and L. F. Chi, *Small*, 2014, **10**, 4865–4873.